CRYSTAL GROWTH & DESIGN

pubs.acs.org/crystal

Article

Chirality and Spin Crossover in Iron(II)−Octacyanidorhenate(V) Coordination Polymers Induced by the Pyridine-Based Ligand's Positional Isomer

Published as part of a Crystal Growth and Design virtual special issue on Molecular Magnets and Switchable Magnetic Materials

Tomasz Charytanowicz, Katarzyna Dziedzic-Kocurek, Kunal Kumar, Shin-ichi Ohkoshi, Szymon Chorazy,* and Barbara Sieklucka*

Cite This: *Cryst. Growth Des.* 2023, 23, 4052−4064

Read Online

ACCESS | Metrics & More | Article Recommendations | Supporting Information

ABSTRACT: We present two novel coordination polymers based on octacyanidorhenate(V) metalloligands and Fe(II) complexes with two different positional isomers of a benzylpyridine ligand, namely 3-benzylpyridine (3-benzpy) that leads to a two-dimensional $\{[Fe^{II}(3\text{-benzpy})_4]_3[Re^{V}(CN)_8]_2\}\cdot 2H_2O$ (**1**) coordination network and 4-benzylpyridine (4-benzpy) giving a three-dimensional $\{[Fe^{II}(4\text{-benzpy})_4]_5[Re^{V}(CN)_8]_3\}(ClO_4)\cdot 2(4\text{-benzpy})\cdot 6H_2O\cdot MeOH$ (**2**) coordination framework. **1** is a layered coordination polymer of a honeycomb topology, crystallizing in the centrosymmetric space group, which exhibits only residual thermal spin-crossover (SCO) effect on Fe(II) complexes at low temperatures. The lack of a significant SCO effect is probably caused by strong supramolecular interactions which do not allow the coordination framework to undergo the structural change required by the spin transition. On the other hand, **2** crystallizes as the chiral, cationic three-dimensional pillared cyanido-bridged framework, consisting of coordination layers of a deformed square grid topology, further bonded together by additional Fe(II) complexes. The structure is completed by noncoordinated 4-benzpy, water, and methanol molecules, as well as perchlorate counterions. The chiral character of the structure of **2** was confirmed by the single-crystal X-ray diffractions studies and the second-harmonic generation (SHG) effect detected at room temperature. **2** exhibits a pronounced two-step, and incomplete thermal SCO effect of embedded Fe(II) complexes. The intricate course of the spin transition in **2** is related to the presence of five crystallographically distinguishable Fe(II) centers with different supramolecular environments. The first noticeable SCO step is realized by the two Fe(II) complexes undergoing the spin transition between 250 and 150 K, while the second is related to the incomplete spin transition of one type of remaining Fe(II) complexes. Therefore, **2** is a rare example of a chiral SCO material showing also the nontrivial course of the spin transition. These properties were achieved by the subtle modification of the pyridine-based ligand indicating the advantage of iron(II)−octacyanidorhenate(V) systems in the formation of functional spin transition materials.

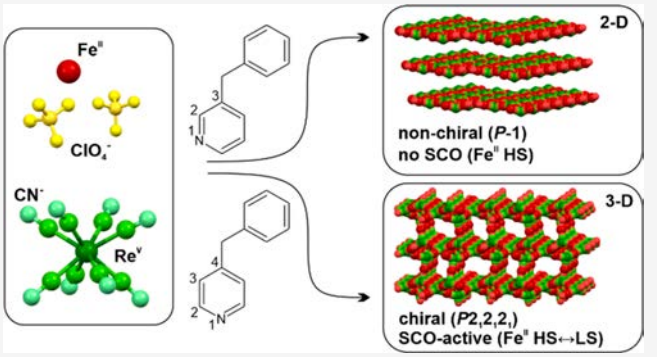

INTRODUCTION

A broad scientific interest is devoted to dynamic molecular materials revealing the switching of physical properties by external stimuli.[1−9] This is due to their applications in sensors, information storage, energy conversion, and others.[10−15] One of the attractive groups of switchable materials consists of spin-crossover-active (SCO-active) coordination compounds employing 3d metal complexes, e.g., $Fe^{II/III}$, Co^{II}, and Mn^{III}. They exhibit externally tunable transitions between high spin (HS) and low spin (LS) states.[16−20] Many physical properties, including magnetic signal or sample color, change upon the spin transition, which can be induced by temperature, light, pressure, or chemical stimuli.[20−28] The various courses of the SCO effect are observed depending on the framework and the type of SCO-active complex. This includes cooperative spin transition leading to the thermal hysteresis loop for the usage in memory devices, gradual SCO applicable for sensing, or the stepwise SCO that can appear in the systems built of two or

Received: December 9, 2022
Revised: May 2, 2023
Published: May 15, 2023

more different SCO-active metal centers, opening the route to expand data storage applications.[29−38]

Among numerous families of spin-crossover materials, the diversity of spin transition characteristics was presented for heterometallic coordination polymers based on Fe(II) complexes combined with polycyanido complexes of transition metals. This can be exemplified by Hofmann-type frameworks composed of di- or tetracyanidometallates, $[M^{I}(CN)_2]^-$ (M = Au, Ag) or $[M^{II}(CN)_4]^{2-}$ (M = Ni, Pd, Pt), and Fe(II) complexes with pyridine derivatives.[39−45] In these networks, the polycyanidometallates serve as linkers between Fe(II) nods. The proper N-donor ligands and N atoms of cyanido ligands ensure the optimal $\{N_6\}$ coordination environment for Fe^{2+} ions enabling the occurrence of the SCO of various parameters depending on the used organic ligand and cyanido complex. Moreover, the Hofmann-type networks are typically porous, providing a strong influence of the removal/exchange of the solvent molecules on the magnetic properties.[41−45] We and other groups modified the related strategy toward SCO materials using octacyanido complexes of transition metals, $[M^{IV/V}(CN)_8]^{4-/3-}$ (M = Nb, Mo, W, Re), instead of di/tetracyanidometallates.[35,46−58] Such an approach can preserve a required $\{N_6\}$ coordination of Fe(II) complexes, allowing us to induce the more diverse set of molecule-based architectures, including coordination clusters,[56,47] layers,[49,55] and complicated three-dimensional (3-D) cyanido-bridged frameworks.[52,53] Recently we focused on the octacyanidorhenate(V) ion, $[Re^{V}(CN)_8]^{3-}$, which was successfully used for the synthesis of coordination clusters and coordination polymers incorporating SCO-active Fe(II) sites.[49,55,57,58] In this context, we showed a 2-D $Cs\{[Fe^{II}(3\text{-cyanopyridine})_2][Re^{V}(CN)_8]\}\cdot H_2O$ framework exhibiting a hysteretic, two-step SCO effect switchable by temperature, light, and pressure.[49] Moreover, the octacyanidometallate-based coordination networks were found to be the source of chiral SCO materials where symmetry breaking is achieved by the bulky organic ligand without the usage of the enantiopure ligand.[52,55] Such materials exhibit the spectacular switching of the second-harmonic polarization plane in the chiral $Fe(II)-[Nb^{IV}(CN)_8]^{4-}$ framework.[52] In this regard, we decided to continue our research on octacyanidorhenate(V)-based coordination polymers with bulky pyridine-type ligands, exploring their potential role in the generation of the SCO effect and the chiral structure. To demonstrate the critical role of the detailed structure of the used ligand, we employed two positional isomers of benzylpyridine ligands differing only in the position of the bulky substituent. As a result, we present two coordination polymers, $\{[Fe^{II}(3\text{-benzpy})_4]_3[Re^{V}(CN)_8]_2\}\cdot 2H_2O$ (**1**) and $\{[Fe^{II}(4\text{-benzpy})_4]_5[Re^{V}(CN)_8]_3\}(ClO_4)\cdot 2(4\text{-benzpy})\cdot 6H_2O\cdot MeOH$ (**2**) (3-benzpy = 3-benzylpyridine, 4-benzpy = 4-benzylpyridine). The subtle change in the ligand's structure resulted in very different structural and magnetic properties, the 2-D nonchiral coordination network with only residual thermal SCO effect in **1**, and the 3-D chiral framework with the two-step, incomplete, thermal SCO effect in **2**. The differences between the compounds and the course of the spin transition in **2** were investigated using X-ray diffraction and various spectroscopic techniques.

EXPERIMENTAL SECTION

Starting Materials. Iron(II) perchlorate hydrate, $Fe(ClO_4)_2\cdot 6H_2O$ (CAS: 335159-18-7, for the sake of calculations considered as hexahydrate), $NaClO_4$ (CAS:7601-89-0), L-ascorbic acid (CAS: 50-81-7), and 4-benzylpyridine (CAS: 2116-65-6) were purchased from Sigma-Aldrich, while 3-benzylpyridine (CAS: 620-95-1) was purchased from Tokyo Chemical Industry. All of them were used as received without further purification. The precursor salt of $TBA_3[Re^{V}(CN)_8]$ (TBA = tetrabutylammonium cation) was prepared following a previously reported, two-step synthetic procedure,[57] which employs commercial potassium hexachlororhenate(IV), $K_2[Re^{IV}Cl_6]$ (CAS: 16940-97-9) and tetrabutylammonium cyanide (CAS: 10442-39-4) as starting materials (both purchased from Sigma-Aldrich).

Synthesis and Basic Physicochemical Characterization. *Synthesis of 1.* An 11.0 mg portion of $Fe(ClO_4)_2\cdot 6H_2O$ (0.03 mmol) and 5.0 mg of L-ascorbic acid (0.03 mmol) were dissolved in 2.0 mL of distilled water. Then a 3 mL volume of water/methanol solution (in the ratio 1:2, v/v) was layered onto the obtained solution. Afterward, a 2.0 mL volume of the methanol solution of $TBA_3[Re^{V}(CN)_8]$ (22.4 mg, 0.02 mmol) and 3-benzpy (20.3 mg, 0.12 mmol) was added as a third layer. After that, the vial was closed and left undisturbed for 2 weeks in a dark place. Then green crystals of **1** appeared. The composition of **1**, $\{[Fe^{II}(3\text{-benzpy})_4]_3[Re^{V}(CN)_8]_2\}\cdot 2H_2O$, was determined by a single-crystal X-ray diffraction (SC-XRD) analysis, together with the thermogravimetric (TG, Figure S2) and CHN analyses. The obtained product is stable in the air. Yield: 4.4 mg, 15%. The IR spectrum of **1** (Figure S1) confirms the presence of the CN^- ligand (cyanido stretching vibrations: 2167 and 2056 cm^{-1} are related to both bridging and terminal cyanido ligands of $[Re(CN)_8]^{3-}$ moieties). Elem. anal. calcd for $Fe_3Re_2C_{160}N_{28}O_2H_{136}$ (**1**, M_w = 3022.9 $\cdot mol^{-1}$): C, 63.6%; H, 4.5%; N, 13.0%. Found: C, 63.2%; H, 4.4%; N, 13.1%.

Synthesis of 2. A 11.0 mg portion of $Fe(ClO_4)_2\cdot 6H_2O$ (0.03 mmol), 42.3 mg of $NaClO_4$ (0.35 mmol), and 5.0 mg of L-ascorbic acid (0.03 mmol) were dissolved in 1.5 mL of distilled water. Then a 2.5 mL volume of water/methanol solution (in the ratio 1:2) was layered onto the obtained solution. Afterward, a 1.5 mL volume of the methanol solution of $TBA_3[Re^{V}(CN)_8]$ (22.4 mg, 0.02 mmol) and 4-benzpy (20.3 mg, 0.12 mmol) was added as a third layer. After that, the vial was closed and left undisturbed for 2 weeks in a dark place. Then green crystals of **2** appeared. The composition of **2**, $\{[Fe^{II}(4\text{-benzpy})_4]_5[Re^{V}(CN)_8]_3\}(ClO_4)\cdot 2(4\text{-benzpy})\cdot 6H_2O\cdot MeOH$, was determined by an SC-XRD analysis, together with the TG (Figure S2) and CHN analyses. The obtained product is stable in the air. Yield: 3.7 mg, 11%. The IR spectrum of **2** (Figure S1) confirms the presence of the CN^- ligand (cyanido stretching vibrations: 2172 cm^{-1}, 2158 cm^{-1}, and 2147 cm^{-1} are related to both bridging and terminal cyanido ligands of $[Re(CN)_8]^{3-}$ moieties). Elem. anal. calcd for $Fe_5Re_3Cl_1C_{289}N_{46}O_{10}H_{254}$ (**2**, M_w = 5388.7$\cdot mol^{-1}$): C, 64.0%; H, 4.8%; N, 11.9%. Found: C, 63.8%; H, 4.5%; N, 12.1%.

X-ray Diffraction Methods. For a single-crystal X-ray diffraction (SC-XRD) analysis, a crystal of **1** was taken directly from the mother solution, dispersed in Apiezon N grease, mounted on the Micro Mounts holder, and measured at T = 100(2) K, using a Bruker D8 Quest Eco Photon50 CMOS diffractometer equipped with graphite monochromatic Mo Kα radiation. For **2**, the preparation procedure was the same but a Bruker D8 Venture diffractometer was employed, and measurements (due to the occurrences of the spin crossover effect) at 100(2), 150(2), and 250(2) K were performed. All structures were solved by an intrinsic phasing method using SHELXT-2014/5 and refined following a weighted full-matrix least-squares method on F^2 using SHELX-2018/3.[59] The refinement procedure was conducted using WinGX (ver. 2014.1) integrated software. All non-hydrogen atoms were refined anisotropically. Hydrogen atoms of organic ligands were modeled using a riding model. The hydrogen atoms of solvent molecules of crystallization were not added due to insufficient data quality. For some of the 4-benzpy ligands of **2**, especially at higher temperatures, it was not possible to model the side chains of the ligands, which was due to the serious structural disorder of these flexible organic groups. It was also necessary to apply a series of ISOR, DFIX, and DELU restraints on the part of non-hydrogen atoms to ensure the convergence of the refinement procedure. Full details of crystal data and structure refinement are gathered in Tables S1 and S2, and detailed structure

https://doi.org/10.1021/acs.cgd.2c01462
Cryst. Growth Des. 2023, 23, 4052−4064

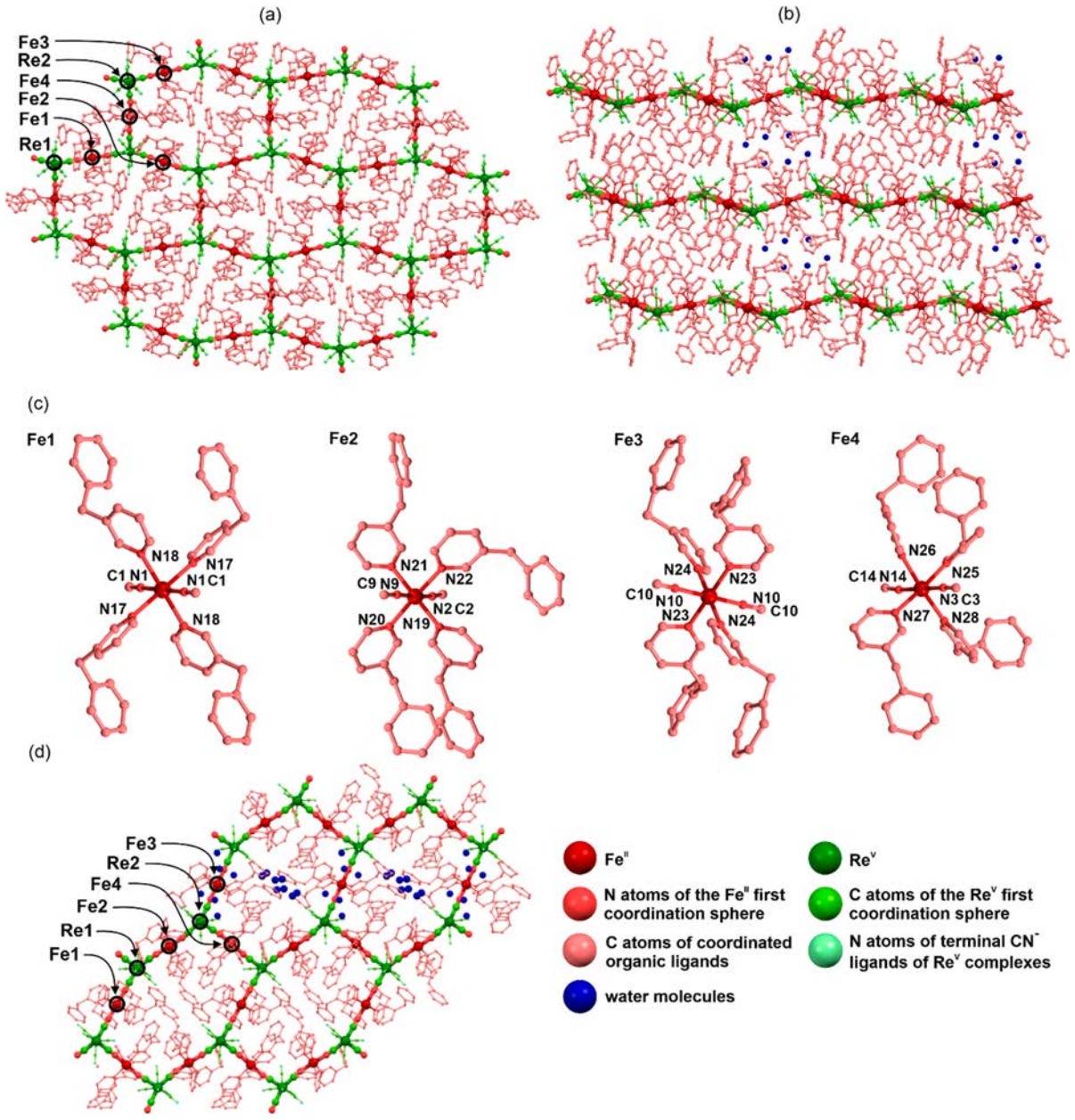

Figure 1. Representative views of the crystal structure of **1** crystallizing in the $P\bar{1}$ space group: a single coordination layer (a), the supramolecular arrangement of coordination layers and water molecules of crystallization (b), the insight into the first coordination spheres of Fe(II) complexes (Fe1, Fe2, Fe3, and Fe4 metal sites) with the labeling schemes for the selected atoms (c), and the more detailed view on the fragment of the coordination layer and the interstitial water molecules, shown together with the color code for the atoms present in the whole figure (d). The hydrogen atoms are omitted for clarity. Additional visualizations of the crystal structure of **1** are presented in Figures S3 and S5.

parameters can be found in Tables S3 and S4, while the respective asymmetric units are shown in Figures S3 and S4. CCDC reference numbers are 2224670 for **1** whereas they are 2224673, 2224672, and 2224671 for **2** at 100(2), 150(2), and 250(2) K, respectively. Structural figures were prepared with Mercury 2021.2.0 software. Powder X-ray diffraction (P-XRD) patterns were measured using a Bruker D8 Advance Eco powder X-ray diffractometer equipped with a Cu Kα radiation source. A capillary spinning add-on was used.

Physical Techniques. Infrared absorption spectra were measured on selected single crystals using a Nicolet iN10 MX FTIR microscope. CHN elemental analyses were performed on an Elementar Vario Micro Cube analyzer. The thermogravimetric (TG) curves were gathered under a nitrogen atmosphere on the air-dried polycrystalline samples using a TG209 F1 Libra TG analyzer with Al pans as holders. Magnetic properties were investigated using an MPMS-3 Evercool magnetometer. The magnetic measurements for **1** and **2** were carried out for air-dried samples, covered by paraffin oil (nujol), and further sealed in polycarbonate capsules containing cotton wool, which was used for the stabilization of the samples. Magnetic data were corrected for the diamagnetic contributions from the sample holder and the samples themselves. The transmission ^{57}Fe Mössbauer spectra were collected using a Wissel spectrometer with a bath liquid nitrogen cryostat at six selected temperatures. The temperature stabilization was better than 0.1 K. The polycrystalline sample for these spectroscopic measurements was prepared by grinding microcrystals, which were further mixed with cellulose powder and sealed by Kapton foils in a copper ring. Mössbauer spectra were fitted with the use of the WinNormos-for-Igor software package, assuming a Lorentzian shape of the resonance lines, i.e., the saturation effects were not included. Two quadrupole doublets (or three at 150 and 100 K) were considered in the fit, assigned to the HS Fe^{II} and LS Fe^{II} states, even though there are five distinguishable positions of Fe atoms in the

https://doi.org/10.1021/acs.cgd.2c01462
Cryst. Growth Des. 2023, 23, 4052−4064

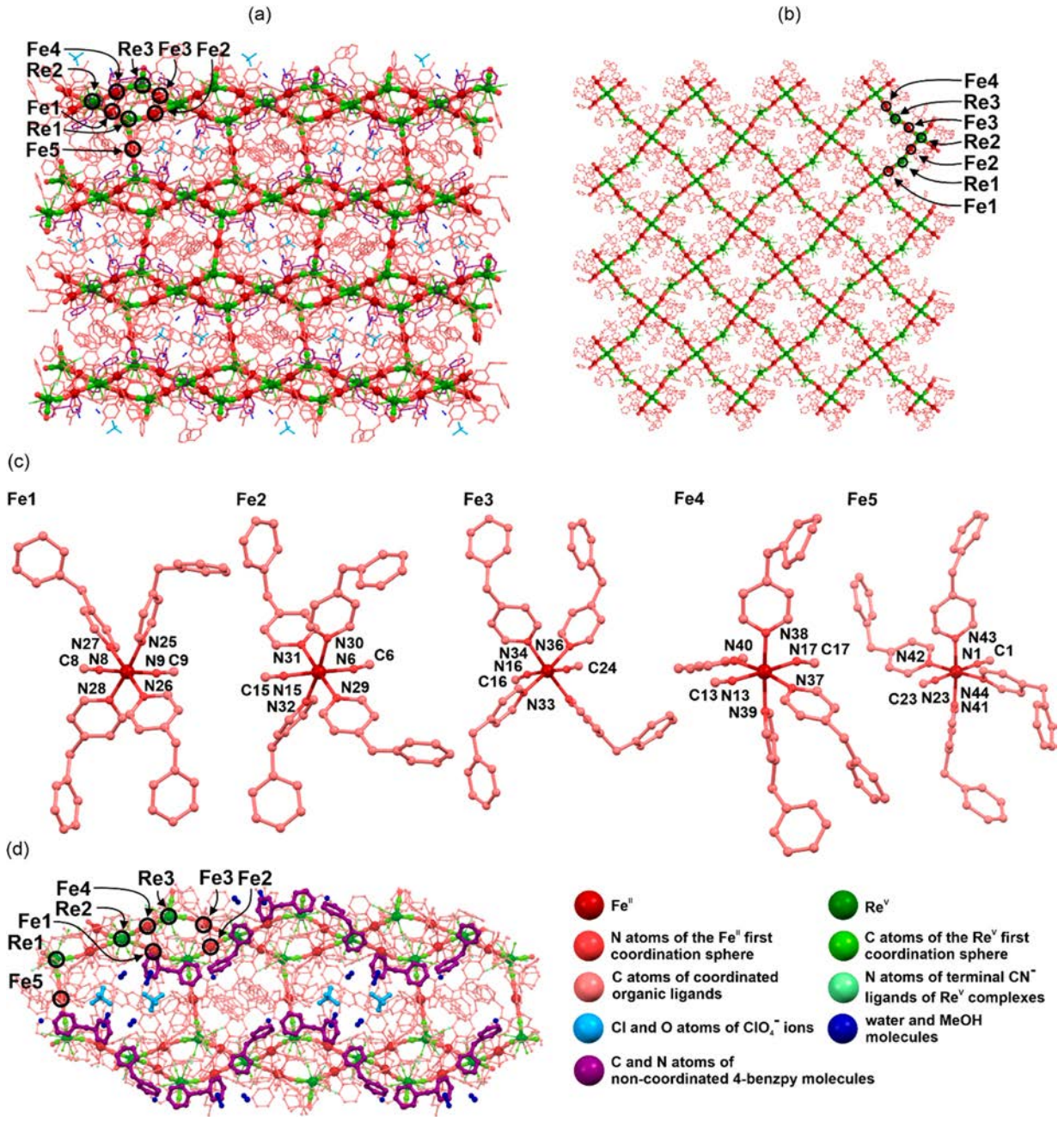

Figure 2. Representative views of the crystal structure of **2** crystallizing in the $P2_12_12_1$ space group with a Flack parameter of 0.0287(17): the side view on the pillared three-dimensional (3-D) coordination framework (a), a single coordination layer being the component of the 3-D coordination network (b), the insight into the first coordination spheres of Fe(II) complexes (Fe1, Fe2, Fe3, Fe4, and Fe5 metal sites) with the related atom labeling schemes (c), and a more detailed view on the fragment of the coordination framework, noncoordinated 4-benzpy molecules, and interstitial solvent molecules, shown together with the color code for the atoms present in the whole figure (d). The hydrogen atoms are omitted for clarity. The structural data gathered at 100(2) K was used to show the crystal structure here. Additional visualizations of the crystal structure of **2** are presented in Figures 3, S4, and S6–S9.

studied material. The relative fractions of the HS vs LS states were determined from the ratio of the areas of the corresponding doublets, which means that equal recoil-free fractions of iron in both spin states were assumed. To determine the SHG activity, **2** was characterized by power-dependent and wavelength-dependent measurements, using a 1040 nm femtosecond laser as incident fundamental light. For the first measurement, the incident laser intensity was tuned with a linear increment from zero, while for the latter measurement, the detection wavelength was adjusted by the monochromator. The SH signal was detected in a reflection mode. A powder sample of **2** was investigated in the SHG experiment, as single crystals large enough for the related measurements of SH light could not be isolated. To quantify the SH intensities generated by the investigated samples, a potassium dihydrogen phosphate (KDP) pellet was used as a reference sample.

Calculations. Continuous shape measure (CSM) analysis for the six-coordinated Fe^{II} complexes and eight-coordinated Re^{V} complexes in **1** and **2** was executed using SHAPE software ver. 2.1.[60,61]

RESULTS AND DISCUSSION

Structural Studies. Green crystals of **1** and **2** were obtained by slow diffusion of methanol solutions containing $TBA_3[Re(CN)_8]$ and the appropriate ligand (3-benzpy for **1** and 4-benzpy for **2**) to a water solution of $Fe(ClO_4)_2$ and L-

https://doi.org/10.1021/acs.cgd.2c01462
Cryst. Growth Des. 2023, 23, 4052−4064

ascorbic acid (applied to prevent the oxidation of Fe^{2+} ions). In the case of **2**, an additional portion of $NaClO_4$ was necessary to ensure the phase purity of the sample, as without $NaClO_4$ some small amounts of red crystals of the other product were observed (which could not be structurally characterized due to the low crystal quality). Both of the obtained materials were characterized by infrared (IR) spectroscopy which revealed the presence of bridging and terminal cyanido ligands of $[Re^{V}(CN)_8]^{3-}$ moieties (Figure S1). To determine the structures of **1** and **2**, selected crystals of each compound were investigated by the SC-XRD technique at 100(2) K (Tables S1 and S2). Compound **1** crystallizes in the centrosymmetric $P\bar{1}$ space group of the triclinic crystal system, while **2** crystallizes in the noncentrosymmetric $P2_12_12_1$ space group of the orthorhombic system. The exact formulas of both compounds have been obtained as a result of structural studies together with CHN and TG analysis (Figure S2), resulting in air-stable compositions of $\{[Fe^{II}(3\text{-benzpy})_4]_3[Re^{V}(CN)_8]_2\}\cdot 2H_2O$ (**1**) and $\{[Fe^{II}(4\text{-benzpy})_4]_5[Re^{V}(CN)_8]_3\}(ClO_4)\cdot 2(4\text{-benzpy})\cdot 6H_2O\cdot MeOH$ (**2**). Compound **1** is composed of wavy, bimetallic coordination layers of $\{[Fe^{II}(3\text{-benzpy})_4]_3[Re^{V}(CN)_8]_2\}$ and water molecules located between them (Figures 1, S3, and S5, Tables S1, S3, S5, and S6). These coordination layers reveal a honeycomb topology consisting of 12-metal $\{Fe_6Re_6\}$ hexagons of alternately arranged cyanido-bridged Fe^{II} and Re^{V} complexes. There are two crystallographically independent Re^{V} complexes (Re1 and Re2) and four such Fe^{II} complexes (Fe1, Fe2, Fe3, and Fe4) in **1**; however, two of them are placed at the special crystallographic positions of the unit cell (Figure S3): (a) Fe1 site at the (0.5, 0, 1) position (the edge of the unit cell) and (b) Fe3 site at the (0.5, 1, 0.5) position (the wall of the unit cell). As a result, for the whole unit cell, the following numbers of Fe centers appear: 1 × Fe1 (4 × Fe1 centers at the edges of the unit cell belonging to four neighboring unit cells), 2 × Fe2, 1 × Fe3 (2 × Fe3 centers at the walls of the unit cell belonging to two neighboring unit cells), and 2 × Fe4; this provides the metal composition of $\{Fe_6Re_4\}$ for the whole unit which can be simplified to $\{Fe_3Re_2\}$ given in the general formula of this compound. For both Re^{V} complexes, three of eight available cyanido ligands are used as molecular bridges that link Fe^{II} and Re^{V} centers while the remaining five cyanido ligands are terminal. The geometry of Re^{V} centers can be described as a triangular dodecahedron (Table S6). All four Fe(II) complexes reveal an octahedral geometry with four N atoms of 3-benzpy ligands in the equatorial positions and two N atoms of cyanido ligands positioned axially in the trans-configuration (Figure 1c, Table S5). The average Fe−N bond lengths for Fe1, Fe2, Fe3, and Fe4 are 2.22, 2.10, 2.19, and 2.19 Å, respectively (Table S3). For Fe1, Fe3, and Fe4, those values are typical for HS Fe(II) complexes, while for Fe2, the values of Fe−N bond lengths suggest the partial occurrence of the spin transition for this complex at 100 K.[1,32] Between the coordination layers, there are water molecules of crystallization and the side chains of 3-benzpy ligands (Figures 1b and S5). One can notice two types of spaces between coordination layers, the first densely filled with organic side chains of 3-benzpy ligands and the second where the side chains of organic ligands create a cavity in which the solvent molecules reside (Figure 1b and 1d). Such behavior results from the highly hydrophobic character of the organic ligand forcing the water molecules to accumulate together to create a rather limited network of hydrogen bonds which is concentrated only in the mentioned cavities.

The change in the position of the substituent within the ligand from 3-benzpy to 4-benzpy leads to a dramatic change in the structure. Compound **2** crystallizes as a chiral, cationic three-dimensional (3-D) pillared coordination framework. It consists of coordination layers of a deformed square grid topology, which are linked together through additional Fe(II) complexes (Figures 2, S4, and S6−S9, Tables S2 and S4). The charge of the framework is compensated by ClO_4^- anions placed in the channels of the structure (Figure S8). The coordination layer component of the structure of **2** consists of 16-metal $\{Fe_8Re_8\}$ squares built of alternately arranged cyanido-bridged Fe^{II} and Re^{V} complexes (Figure 2b). One can notice two types of layered components that are shifted from one another (Figure S7). The crystal structure is completed with noncoordinated ligands, ClO_4^- ions, and solvent molecules (Figures 2d and S8). Free molecules of 4-benzpy are located tightly around layered parts of the framework while perchlorate ions together with water and methanol molecules are located between coordination layers in the channels of the structure. It was impossible to locate all of the possible solvent molecules pointed out by TG and CHN analyses which is due to their partial delocalization and weak noncovalent interaction with the network. The coordination framework of **2** is chiral and enantiomorphic as it crystallizes in the $P2_12_12_1$ space group with the Flack parameter close to zero (Tables S2). Therefore, we gathered the structural data for one of the possible enantiomers. As no chiral ligand was used, the chirality appears as the result of the spontaneous resolution process; thus, the crystalline sample **2** is a mixture of the crystals of two enantiomorphs. Due to the insufficient quality of most of the crystals of **2**, it was impossible to accomplish good-quality X-ray diffraction for this second enantiomer. Nevertheless, the chiral structure of **2** is fully confirmed by the X-ray diffraction data presented and, further, by the nonzero SHG activity supporting the proper determination of the noncentrosymmetric $P2_12_12_1$ space group (see below). We checked that the powder sample of **2** does not exhibit a detectable circular dichroism (CD) spectrum in the UV−vis range corresponding to the absorption of the material; this suggests that the bulk sample of **2** consists of an equimolar mixture (conglomerate) of the crystals of two enantiomers. For such a case, the CD signal vanishes, as the crystals of two enantiomers give the opposite sign of the related optical response but the SHG effect, related to the lack of the inversion center in the crystal structure, appears.[52,62−65]

The chirality of **2** can be visualized by comparison with the second hypothetical enantiomer (Figures 3 and S9). From this comparison, one can notice that the chirality appears for the coordination skeleton which is related to the connections between Fe(II) and Re(V) complexes. For instance, four different Fe sites (Fe1, Fe2, Fe3, and Fe4) are attached to each Re2 site; thus, considering only bridging ligands, this Re2 site can be described as the distorted tetrahedral entity of the {M(ABCD)} type which is an intrinsically chiral type of metal complex. Therefore, the bulky character of the 4-benzpy ligand was found to affect the structure in a way that the coordination skeleton becomes chiral, including the appearance of chirality even at the very molecular level of selected metal complexes. It is important to add here that further exploration of the observed chirality, e.g., toward the investigation of chiroptical or magnetochiral effects, will need the detection and manual separation of two types of enantiomorphic crystals from the obtained conglomerate.[52]

https://doi.org/10.1021/acs.cgd.2c01462
Cryst. Growth Des. 2023, 23, 4052−4064

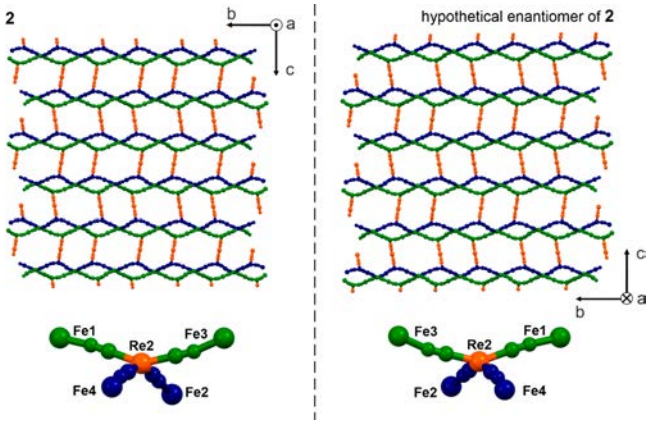

Figure 3. Views of the chiral, enantiomorphic character of the structure of **2** including the view of the coordination skeleton (top) as well as the coordination environment around Fe(II) centers (bottom). For a better visualization of the enantiomorphic character of **2**, the structure for the crystal of the hypothetical enantiomer of **2** was shown on the right side (see the text for details).

From the viewpoint of the possible SCO effect, we analyzed more precisely the metal complexes embedded in **2** (Figure 2). There are three distinguishable Re (Re1, Re2, and Re3) and five Fe (Fe1, Fe2, Fe3, Fe4, and Fe5) centers in **2**. Complexes Re1 and Re3 link three surrounding Fe^{II} complexes via cyanido bridges, while five of their cyanido ligands remain terminal. These complexes are located on the sides of the coordination squares, using two cyanido bridges to construct the layered component of the framework, while one remaining cyanido bridge is used to bind the adjacent coordination layer through the Fe(II) complex. The Re2 complex lies on the vertex of the coordination square, employing four of its cyanido ligands to construct the neighboring coordination squares, while the four remaining cyanido ligands remain terminal. All Re^{V} centers adapt the geometry of a triangular dodecahedron (Table S6), while the geometry of all Fe^{II} centers can be ascribed as octahedral (Table S5). Every Fe(II) complex consists of equatorially aligned four 4-benzpy ligands and two cyanido ligands in trans-configuration (Figure 2c). Complexes of Fe1, Fe2, Fe3, and Fe4 construct the coordination squares, employed as linkers between Re^{V} centers, while Fe5 is used as a bridge to connect two adjacent layered fragments of the framework. At 100 K, the average Fe−N bond lengths are 2.00, 2.19, 2.12, 2.20, and 2.01 Å for Fe1, Fe2, Fe3, Fe4, and Fe5, respectively (Table S4). The bond length values for Fe1 and Fe5 indicate the Fe(II) LS state, while those for Fe2 and Fe4 suggest the HS state. The Fe−N bond lengths in Fe3 suggest the partial occurrence of the SCO effect for this complex.[1,32]

To study the possible SCO effect, suggested by crystal data at 100 K and by the change of the color of crystals upon cooling (from the green one obtained in the synthesis to the red color at low temperatures, Table S2), a series of *T*-dependent X-ray diffraction structural analyses were performed. The temperatures of measurements were chosen concerning temperature-dependent magnetic curves (see Magnetic Properties below). Besides the original experiment at 100(2) K (see above), the measurements were executed at 150(2) and 250(2) K. The results are presented in Tables 1, S2, and S4−S6. For all studied temperatures, there is no change in the crystallographic system or space group; however, the metric parameters of the structure significantly change. The *a*, *b*, and *c* lattice constants at 100 K are 27.9593(11), 28.8508(11), and 31.1577(11) Å, respectively (Table S2). Upon heating the crystal to 150 K, one observes a slight increase of the lattice parameters to 28.0422(10), 28.9484(10), and 31.2294(10), which is related to the typical positive thermal expansion effect but the partial SCO effect can also contribute. Further heating to 250 K results in a relatively huge increase of the lattice constants up to 28.2678(19), 29.1558(19), and 31.617(2) Å, which cannot be simply assigned to the thermal expansion; thus, it is due to the occurrence of the spin transition. The biggest change is observed for the *c* parameter, which corresponds to the increased interlayer distance. This suggests that the spin transition is rather occurring for the Fe5 complex connecting the adjacent layered fragments of the network (Figure 2). The shape of the coordination skeleton does not change dramatically upon heating, as depicted by the shape analysis

Table 1. Summary of the Fe−N Bond Lengths for 2 at the Indicated Temperatures[a]

	temperature				temperature		
Fe−N pair (Figure 2)	100 K	150 K	250 K	Fe−N pair (Figure 2)	100 K	150 K	250 K
Fe1−N8	1.933(8)	1.962(8)	2.098(9)	Fe3−N34	2.148(7)	2.191(7)	2.225(8)
Fe1−N9	1.947(8)	1.976(7)	2.105(8)	Fe3−N35	2.153(8)	2.195(8)	2.214(9)
Fe1−N25	2.039(9)	2.061(9)	2.187(11)	Fe3−N36	2.143(8)	2.181(8)	2.222(9)
Fe1−N26	2.030(8)	2.055(8)	2.197(10)	Fe4−N13	2.126(8)	2.127(8)	2.119(8)
Fe1−N27	2.045(8)	2.076(8)	2.216(10)	Fe4−N17	2.156(9)	2.163(8)	2.160(9)
Fe1−N28	2.030(8)	2.043(9)	2.178(11)	Fe4−N37	2.228(10)	2.227(10)	2.232(12)
Fe2−N6	2.126(7)	2.131(7)	2.136(8)	Fe4−N38	2.160(12)	2.162(12)	2.166(13)
Fe2−N15	2.128(7)	2.126(7)	2.128(8)	Fe4−N39	2.212(8)	2.214(8)	2.221(10)
Fe2−N29	2.208(8)	2.214(8)	2.221(10)	Fe4−N40	2.293(10)	2.298(10)	2.259(12)
Fe2−N30	2.215(7)	2.217(7)	2.215(9)	Fe5−N1	1.950(7)	1.969(7)	2.084(9)
Fe2−N31	2.241(8)	2.246(7)	2.243(9)	Fe5−N23	1.958(8)	1.981(8)	2.119(10)
Fe2−N32	2.223(7)	2.226(7)	2.246(9)	Fe5−N41	2.056(7)	2.077(7)	2.218(9)
Fe3−N16	2.052(7)	2.094(7)	2.124(8)	Fe5−N42	2.039(7)	2.063(7)	2.227(9)
Fe3−N24	2.071(8)	2.104(8)	2.129(8)	Fe5−N43	2.054(7)	2.074(7)	2.210(9)
Fe3−N33	2.146(7)	2.185(7)	2.226(9)	Fe5−N44	2.016(8)	2.030(9)	2.181(11)

[a]The values in bold represent the bond lengths of the Fe(II) centers assigned to the significant contribution of the low-spin spin state at the indicated temperatures (see the text for details). The other centers remain almost purely at the high-spin state at the given conditions.

https://doi.org/10.1021/acs.cgd.2c01462
Cryst. Growth Des. 2023, 23, 4052−4064

of the complexes at different temperatures (Tables S5 and S6). Both Fe(II) and Re(V) complexes remain at their original geometry over the whole studied temperature range.

The direct studies of the individual Fe(II) complexes result in a much more detailed view of the SCO effect (Table 1). As mentioned above, at 100 K two Fe(II) complexes (Fe1 and Fe5) revealed the Fe−N bond lengths characteristic for the LS Fe(II) complexes, and two Fe(II) complexes (Fe2 and Fe4) revealed the Fe−N bond lengths characteristic for the HS Fe(II) complexes, while the Fe3 complex revealed the intermediate metric parameters. At 150 K, the average Fe−N bond lengths are 2.03, 2.19, 2.16, 2.20, and 2.03 Å for Fe1, Fe2, Fe3, Fe4, and Fe5, respectively. The Fe−N bond lengths for complexes Fe1 and Fe5 only slightly increased, thus mainly due to the natural thermal expansion effect. The average Fe−N bond lengths almost did not change for complexes Fe2 and Fe4, which can result from the stable HS state of those complexes. The most noticeable change is observed for Fe3; the increase of Fe−N bond lengths in this regime suggests that, upon heating to 150 K, the majority of Fe3 complexes turn into an HS state. At 250 K, the average Fe−N bond lengths are 2.15, 2.20, 2.19, 2.19, and 2.17 Å for Fe1, Fe2, Fe3, Fe4, and Fe5, respectively. Thus, there is a strong increase in the average Fe−N bond lengths for complexes Fe1 and Fe5, which indicates the complete spin transition from LS to HS for these complexes between 150 and 250 K. There is also a further increase of the Fe−N bond lengths for Fe3, which can be explained by the finalization of the spin transition to the HS state. The Fe−N bond lengths for Fe2 and Fe4 remain almost the same, and the related tiny changes in metric parameters for them (both the decrease and increase of the bond lengths) can be related to the accommodation of the whole complexes to the structural changes, arising from spin transitions of Fe1, Fe3, and Fe5 complexes.

The phase purity of bulk samples of both compounds, **1** and **2**, was checked with a powder X-ray diffraction (P-XRD) experiment (Figure 4). The obtained powder patterns match well the respective powder patterns generated from the structural models obtained within the SC-XRD analyses. This proves the phase purity of the bulk samples for **1** and **2**, confirming that the 3-benzpy-to-4-benzpy ligand substitution leads to the above-described change of the structural features for the whole obtained batches of compounds.

Magnetic Properties. **1** and **2** contain Fe(II) complexes with the $\{N_6\}$ coordination environment, which is known to be suitable to observe the SCO effect.[1,32] Moreover, some of the formed Fe(II) complexes exhibit the Fe−N bond lengths characteristic of LS Fe(II) complexes when the crystal was investigated by the SC-XRD method at 100(2) K (see above), which suggests the occurrence of the thermally induced SCO effect. Direct-current (dc) magnetic measurements were carried out to investigate this possibility for both compounds. These studies include temperature-dependent measurements at a constant magnetic field and field-dependent measurements at a constant very low temperature (Figures 5 and S10). For **1**, the $\chi_M T$ value, for the $\{Fe_3Re_2\}$ formula unit, reaches the value of 11.3 $cm^3\ mol^{-1}$ K at room temperature, which fits the range of 10.9−13.0 $cm^3\ mol^{-1}$ K, expected for three, uncoupled, high-spin Fe(II) centers ($S = 2$), with the g factor lying within the range of 2.2−2.4.[49−55] Upon cooling, the $\chi_M T$ value remains stable until 150 K. Below this point, the $\chi_M T$ decreases mildly to 10.5 $cm^3\ mol^{-1}$ K at 55 K, which is the decrease of ca. 7%. Upon further cooling, there is a sharp decrease in the signal to 6.8 $cm^3\ mol^{-1}$ K at 1.8 K (Figure 5a). For the heating of the sample, the shape of the $\chi_M T$ curve remains the same as for the cooling, so no hysterical effects are observed (Figure S10a). The shape of the $\chi_M T$ curve suggests that above 150 K all Fe(II) complexes of **1** are in the high-spin state. The small decrease of the signal in the 150−55 K range suggests the residual, incomplete spin transition for one of the Fe(II) complexes. Such interpretation is supported by the crystallographic data collected at 100 K, as the Fe−N bond lengths for the Fe2 complex are slightly shorter than analogous bond lengths for the other Fe(II) complexes (Table S3). Even though those values are still significantly longer than expected for purely low-spin Fe(II) complex, only a very partial SCO effect is observed. The decrease of $\chi_M T$ value below 55 K can be explained by weak antiferromagnetic (AF) interactions between Fe(II) centers linked by $[Re^V(CN)_8]^{3-}$ moieties, as well as by a zero-field splitting (ZFS) effect on Fe(II) complexes.[49−55] The field-dependent measurements at 1.8 K support the dominant role of AF interactions and the single ion anisotropy at low temperatures, as the M curve (Figure 5a, inset) exhibits a monotonous increase of a signal upon applying the magnetic field, reaching a value of 7.6 μ_B at 70 kOe. This value is far below the 13.2 μ_B expected for three parallel arranged magnetic moments of HS Fe(II) centers ($S = 2$, $g = 2.2$), though the saturation of magnetization is not achieved for the applied field.

For **2**, the $\chi_M T$ value, for the $\{Fe_5Re_3\}$ formula unit, reaches a value of 20.3 $cm^3\ mol^{-1}$ K at 400 K which lies within the range of 18.2−21.6, expected for five uncoupled high-spin Fe(II) centers. The $\chi_M T$ value remains almost stable upon cooling to ca. 250 K when a gradual decrease of the signal is

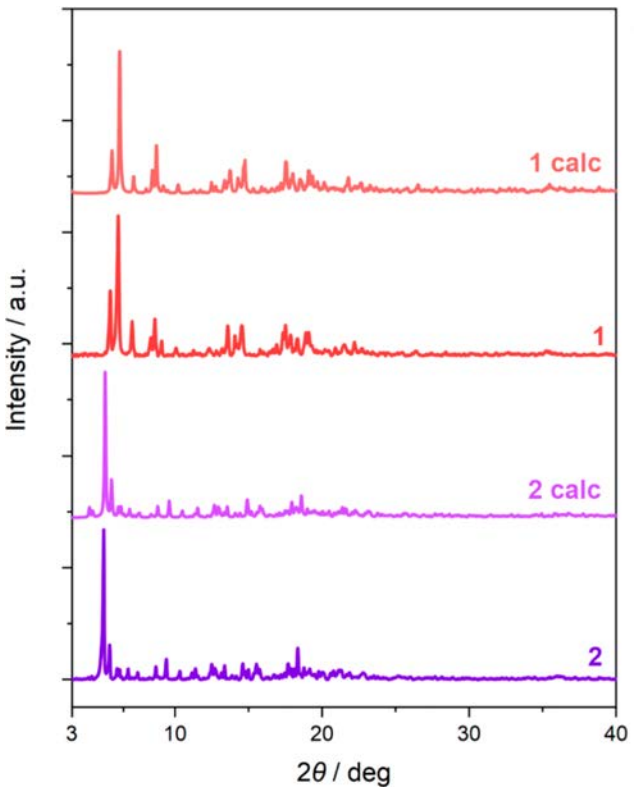

Figure 4. Experimental powder X-ray diffraction patterns of **1** and **2**, compared with the respective powder patterns calculated from the structural models (Figures 1 and 2, and the labels of **1 calc** and **2 calc**, respectively).

https://doi.org/10.1021/acs.cgd.2c01462
Cryst. Growth Des. 2023, 23, 4052−4064

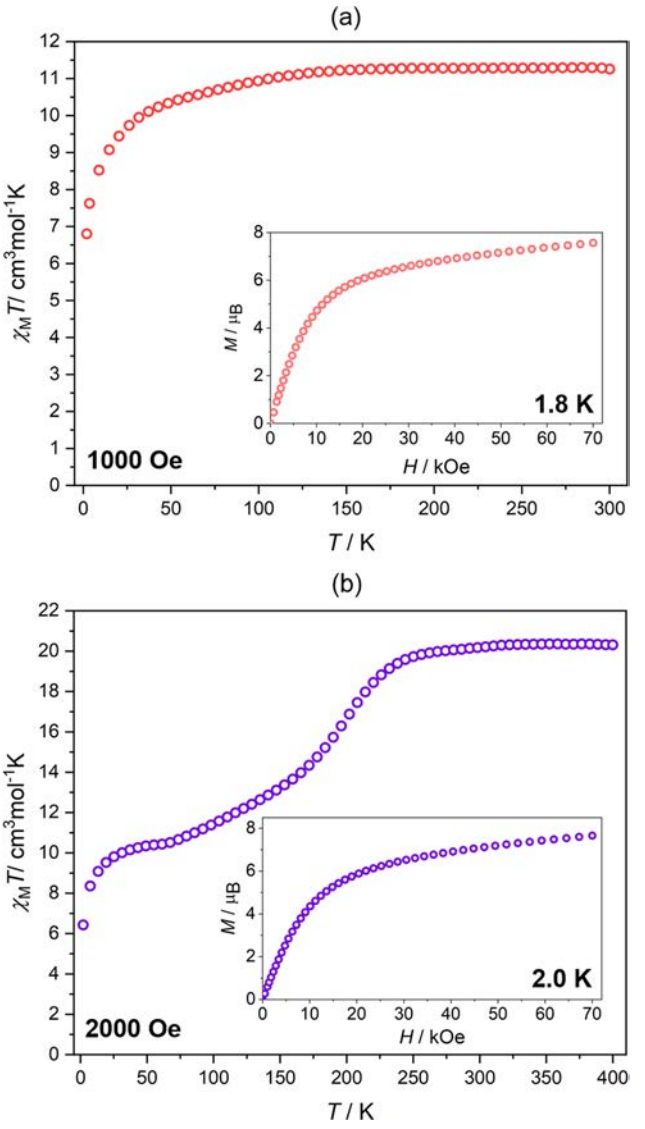

Figure 5. Magnetic properties of **1** (a) and **2** (b), including temperature dependences of the magnetic susceptibility−temperature product, $\chi_M T$ gathered at the indicated dc magnetic fields and the field-dependences of magnetization at the indicated temperatures (the insets).

observed down to 10.4 cm^3 mol^{-1} K at 60 K (ca. 49% decrease, Figure 5b). There are two distinguishable steps in the magnetic curve within the 275−60 K range. The first one is more abrupt and occurs between 250 and 150 K (13.1 cm^3 mol^{-1} K, ca. 36% decrease), with the transition temperature, $T_{1/2}$ around 200 K (Figures 5b, S10b, and S11). The second step is mild and results in a ca. 13% decrease in the $\chi_M T$ value. Below 60 K, there is an abrupt decrease of the signal down to 6.4 cm^3 mol^{-1} K at 2.0 K (Figure 5b). Upon heating of the sample, the shape of the $\chi_M T$ curve is preserved; thus, no hysteretic effects are observed (Figure S10b). The first step in the $\chi_M T$ curve can be ascribed to the spin transition occurring on two of five Fe(II) centers of compound **2**, as the decrease of a signal (ca. 36%) is in good agreement with the decrease expected for two of five Fe(II) complexes undergoing the SCO effect (40%). This explanation is supported by the structural data (Tables 1 and S4) at 150 K, as there are two Fe(II) complexes with the Fe−N bond lengths typical for LS Fe(II) centers (see above). The second step can be explained by the incomplete spin transition occurring on one of the remaining HS Fe(II) centers. The Fe3 center would be a perfect candidate, as at 100 K the average Fe−N bond lengths suggest the partial occurrence of spin transition for this metal center. The advanced structural studies confirm this interpretation, as at 150 K there is an increase of the average Fe−N bond lengths up to 2.19 Å for this complex (see above). The decrease of the $\chi_M T$ signal below 60 K can be, as for **1**, explained by non-negligible AF interactions and the ZFS effect at low temperatures. The field-dependent measurement at 2.0 K shows similar behavior as for **1** (Figure 5b). M reaches a value of 7.7 μ_B at 70 kOe without reaching saturation, which underlines the significant role of AF interactions and the single ion anisotropy at low temperatures. It is important to add here that the heating−cooling cycle of the magnetic measurement for **2** (Figure S10) was performed in the 2−400 K range starting from low temperature (2 K, after quickly cooling the sample without the measurement from room temperature), heating the sample to 400 K, and then cooling back to 2 K. We found that the temperature dependences of the magnetic susceptibility−temperature product for the heating and the subsequent cooling of the sample are identical. Thus, there is no sign of significant changes above 300 K that could be assigned to the thermally induced desolvation process which one can postulate from the course of the TG curve (Figure S2). This suggests that the desolvation of the air-dried sample of **2** does not occur up to 400 K which is due to the protective oil covering the sample for the magnetic measurements (in the TG experiment, the unprotected sample placed in the flow of nitrogen is investigated, see Experimental Section for details). The eventual partial desolvation, which could be related to the removal of the part of solvent molecules of crystallization even for the sample protected by the paraffin oil, does not have a noticeable impact on the magnetic characteristics. It means that the crucial thermal SCO effect is repeatable for the heating−cooling cycle in the 2−400 K range.

^{57}Fe Mössbauer Spectroscopy Characterization for 2.

To further confirm the SCO phenomenon in **2**, a series of temperature-dependent ^{57}Fe Mössbauer spectra were gathered. The results are presented in Figure 6 and Table 2. The spectra at 300 and 250 K share a similar shape and exhibit a single doublet with isomeric shifts (δ_{IS}) of 1.03(1) and 1.16(1) mm·s^{-1}, respectively. The quadrupole splitting (ΔE_Q) values at these temperatures also do not change dramatically, reaching values of 1.72(1) and 2.04(1) mm·s^{-1}, respectively. These spectral parameters are characteristic of HS Fe(II) centers,[32,49−55] which supports the previous interpretation of temperature-dependent dc magnetic and structural studies at those temperatures (Figure 5 and Table 1). The presence of only one doublet, while there are five distinguishable Fe(II) centers in **2**, can be explained by the similar chemical environment of each center. The further cooling of the sample to 200 K leads to the appearance of a second doublet in the Mössbauer spectrum. The observed doublets can be characterized with the δ_{IS} and ΔE_Q values of 1.18(1) and 2.15(1) mm·s^{-1} for the first doublet and 0.46(1) and 0.25(1) mm·s^{-1} for the second one. The parameters of the first doublet are similar to the parameters of the doublet observed at 250 K. Therefore, it can be ascribed to the HS Fe(II) complexes. The newly appearing doublet exhibits much smaller values of δ_{IS} and ΔE_Q which are typical for LS Fe(II) complexes, and stands in perfect agreement with the magnetic measurements, as in

https://doi.org/10.1021/acs.cgd.2c01462
Cryst. Growth Des. 2023, 23, 4052−4064

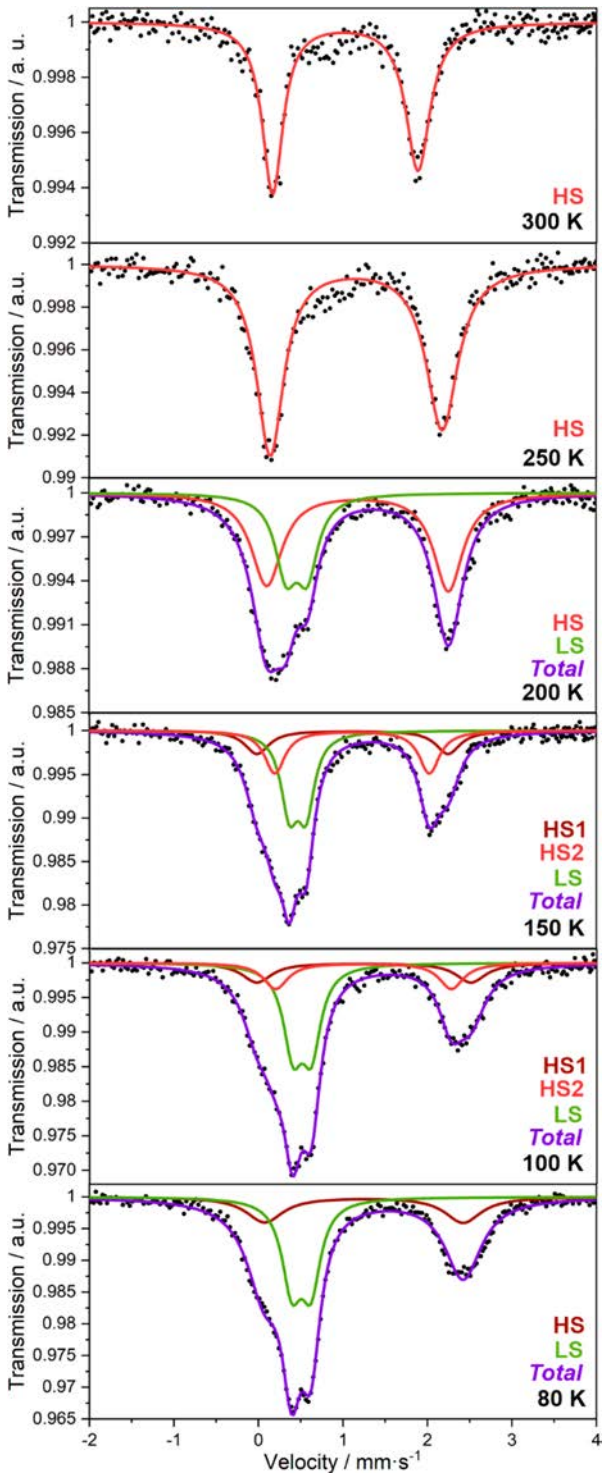

Figure 6. Temperature-variable ^{57}Fe Mössbauer spectra of **2** with the indicated names of three different Fe(II) sites (two high-spin state sites of HS1 and HS2, and one low-spin state site of LS). Experimental data is presented as black points, while the fitted results as solid lines with specific indicated colors for HS and LS contributions and the total fits.

the 200−250 K region the spin transition starts to occur. At 200 K, the contribution of the HS Fe(II) centers is 72%, leaving 28% for the LS Fe(II) centers (Table 2). This agrees with the interpretation of the spin transition occurring gradually mainly for Fe1 or Fe5 centers in the 250−200 K region. After further cooling to 150 K, two different HS sites can be distinguished by the spectra. They are characterized by the δ_{IS} and ΔE_Q values of 1.11(1) and 2.26(3) mm·s^{-1} for the first HS site (HS1) and 1.11(1) and 1.83(2) mm·s^{-1} for the second one (HS2). The parameters of the LS component of the spectra change a little bit, reaching 0.47(1) and 0.20(1) mm·s^{-1} for δ_{IS} and ΔE_Q, respectively. In this step, the fraction of LS Fe(II) complexes increases to 40%, which agrees well with the structural data, as, at 150 K, two out of five Fe(II) centers are in the LS state. This also stays in good agreement with the related decreases of the signals in magnetic data. The Mössbauer spectrum at 100 K exhibits a similar shape as for 150 K. The δ_{IS} and ΔE_Q parameters for both HS doublets increase, reaching 1.25(1) and 2.53(4) mm·s^{-1} for HS1, as well as 1.24(1) and 2.08(3) mm·s^{-1} for HS2, respectively. The low spin doublet is characterized by slightly increased parameters than for 150 K, which are 0.51(1) and 0.22(1) mm·s^{-1} for δ_{IS} and ΔE_Q, respectively. A slight increase of the LS Fe(II) fraction up to 47% is detected, which can be explained by the partial spin transition of the Fe3 center at this temperature (Table 1). These results also agree with magnetic measurements, for which we observed a 43% decrease in the initial signal at 100 K. The further decrease of temperature to 80 K does not change the percentage of each fraction, but at this temperature, it was not possible to distinguish clearly two different HS Fe(II) sites, which can be explained by the similarity of hyperfine interactions parameters of remaining HS sites at this temperature. This feature is confirmed by a line width broadening, reaching 0.53(1) mm·s^{-1}.

Table 2. ^{57}Fe Mössbauer Spectra Parameters for 2

T/K	Fe(II) spin state	δ_{IS}/mm·s^{-1}	ΔE_Q/mm·s^{-1}	fraction/%
295	HS	1.03(1)	1.72(1)	100
	LS	-	-	-
250	HS	1.16(1)	2.04(1)	100
	LS	-	-	-
200	HS	1.18(1)	2.15(1)	72(1)
	LS	0.46(1)	0.25(1)	28(1)
150	HS1	1.11(1)	2.26(3)	26(1)
	HS2	1.11(1)	1.83(2)	34(1)
	LS	0.47(1)	0.20(1)	40(1)
100	HS1	1.25(1)	2.53(4)	28(1)
	HS2	1.24(1)	2.08(3)	25(1)
	LS	0.51(1)	0.22(1)	47(1)
80	HS	1.25(1)	2.35(1)	53(1)
	LS	0.51(1)	0.23(1)	47(1)

Second Harmonic Generation Effect for 2. In addition to the structural, magnetic, and spectroscopic characteristics investigated for **2** revealing the thermal SCO effect, we also studied the possible nonlinear optical (NLO) phenomenon of second harmonic generation (SHG). It was expected for **2**, as it crystallizes in the $P2_12_12_1$ space group belonging to the noncentrosymmetric SHG-active 222 point group.[66−69] Therefore, the powder sample of **2** was irradiated at room temperature with a 1040 nm femtosecond pulse laser as incident fundamental light using a homemade experimental setup, as described previously.[70,71] As a result, we observed the signal around 520 nm that was subsequently studied at power-dependent measurements (Figure 7). The observed signal was found to be proportional to the square of the excitation light intensity, indicating the two-photon process characteristic of the SHG effect. To quantify the observed SH light intensity,

https://doi.org/10.1021/acs.cgd.2c01462
Cryst. Growth Des. 2023, 23, 4052−4064

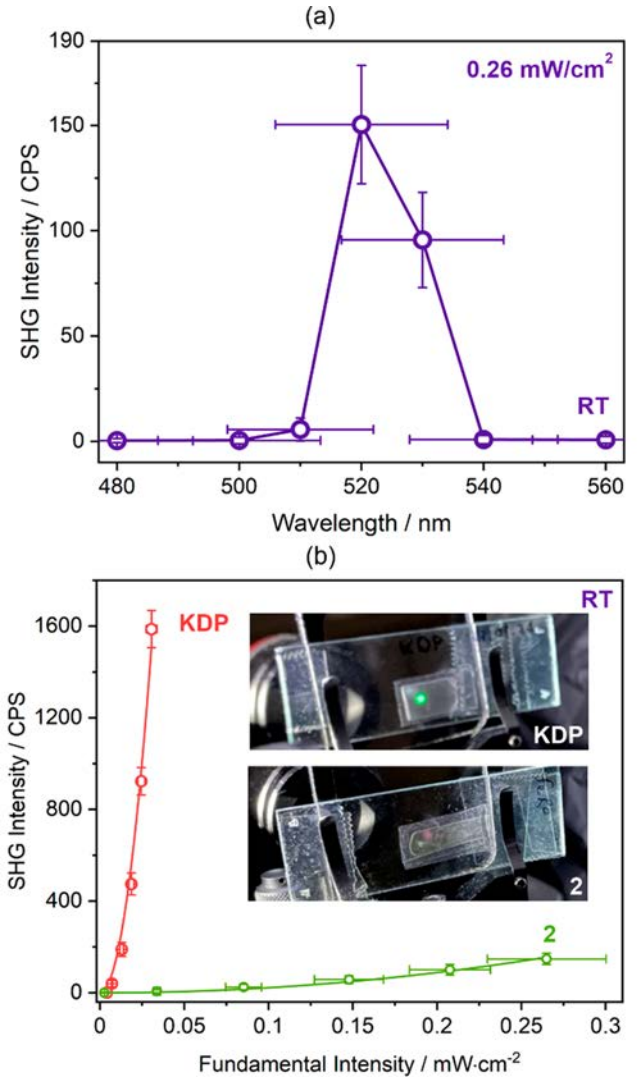

Figure 7. Room-temperature SHG effect under 1040 nm laser irradiation for the powder sample of **2**, represented by the SHG intensity shown in the function of wavelength (a), the related dependence on the excitation intensity (b), and the photo of the sample and the observed SH light (b, the inset). In panel b, the results for the KDP reference samples measured at identical conditions are presented for comparison. In panel b, the solid lines represent the best-fits to quadratic function, proving the SH nature of the detected light (see the text for details).

we used the potassium dihydrogen phosphate (KDP) sample as a reference, measured at the same conditions. The observed SH intensity of **2** reaches only 0.15% of the KDP intensity, indicating a rather weak NLO response from the material which can be ascribed, among others, to the significant structural disorder existing in the framework of **2** as well as to the effects of the powder sample which typically demonstrate worse SHG activity than the large single crystals; however, this SH intensity is non-negligible, reaching the level sometimes observed for the coordination polymers crystallizing, thanks to the spontaneous resolution process, in the $P2_12_12_1$ space group or other noncentrosymmetric space groups.[71−77] Therefore, it further supports the chiral character of the coordination of **2** that was depicted in the structural studies.

CONCLUSIONS

We report two novel coordination frameworks based on octacyanidorhenate(V) ions connected with iron(II) complexes bearing two positional isomers of bulky benzylpyridine ligands. We found a critical role of the position of the bulky substituent on the structural, magnetic, and optical properties of the resulting coordination networks. The 3-benzylpyridine induces the formation of a layered cyanido-bridged framework, crystallizing in the centrosymmetric space group, in which the layers are tightly stacked within the crystal lattice. As the result, despite the proper $\{N_6\}$ coordination environment around Fe(II) metal centers, there is only a residual thermal spin crossover effect, and almost all Fe(II) sites remain in the high spin state for the whole temperature range. On the contrary, the 4-benzylpyridine induces the formation of a unique three-dimensional pillared coordination framework, revealing spontaneously generated chirality observed due to the arrangement within the coordination skeleton. As a result, the NLO property of second harmonic generation could be detected for this material. Moreover, the framework becomes more porous with the large channels filled with various noncoordinated molecules and counterions. The porous character of the resulting network contributes to the observation of the pronounced thermal spin crossover effect with the nontrivial course involving two steps and the incomplete character, consistently observed within the structural, magnetic, and ^{57}Fe Mössbauer effect spectroscopic studies. Our work demonstrates that even the subtle pyridine ligand modification can induce the dramatic variation of structural and magnetic features of spin crossover materials, especially for those based on iron(II)−octacyanidorhenate(V) bimetallic assemblies which are still rarely explored in the research field. The next step of the exploration of these promising heterometallic systems is directed toward their structural and spin transition sensitivity to guest molecules which will be the subject of our future work.

ASSOCIATED CONTENT

Supporting Information

The Supporting Information is available free of charge at https://pubs.acs.org/doi/10.1021/acs.cgd.2c01462.

Infrared (IR) absorption spectra. TG curves. Details of crystal data and structure refinement. An additional set of structural views and structure parameters. Results of continuous shape measure analysis. Additional magnetic characteristics (PDF)

Accession Codes

CCDC 2224670−2224673 contain the supplementary crystallographic data for this paper. These data can be obtained free of charge via www.ccdc.cam.ac.uk/data_request/cif, or by emailing data_request@ccdc.cam.ac.uk, or by contacting The Cambridge Crystallographic Data Centre, 12 Union Road, Cambridge CB2 1EZ, UK; fax: +44 1223 336033.

AUTHOR INFORMATION

Corresponding Authors

Szymon Chorazy − *Faculty of Chemistry, Jagiellonian University, 30-387 Krakow, Poland;* orcid.org/0000-0002-1669-9835; Email: simon.chorazy@uj.edu.pl

Barbara Sieklucka − *Faculty of Chemistry, Jagiellonian University, 30-387 Krakow, Poland;* orcid.org/0000-0003-3211-5008; Email: barbara.sieklucka@uj.edu.pl

Authors

Tomasz Charytanowicz − *Faculty of Chemistry, Jagiellonian University, 30-387 Krakow, Poland;* orcid.org/0000-0002-0803-6046

Katarzyna Dziedzic-Kocurek − *Marian Smoluchowski Institute of Physics, Jagiellonian University, 30-348 Krakow, Poland*

Kunal Kumar − *Department of Chemistry, School of Science, The University of Tokyo, Tokyo 113-0033, Japan;* orcid.org/0000-0002-2626-0615

Shin-ichi Ohkoshi − *Department of Chemistry, School of Science, The University of Tokyo, Tokyo 113-0033, Japan;* orcid.org/0000-0001-9359-5928

Complete contact information is available at: https://pubs.acs.org/10.1021/acs.cgd.2c01462

Author Contributions

The manuscript was written through the contributions of all authors. All authors have given approval to the final version of the manuscript.

Notes

The authors declare no competing financial interest.

■ ACKNOWLEDGMENTS

This work was financed by the National Science Centre, Poland, within the OPUS-20 project (grant no. 2020/39/B/ST5/02815). T. Charytanowicz acknowledges the Polish Ministry of Science and Higher Education for the financial support within the research grant under the "Diamond Grant" program (grant no. DI2018 018148).

■ REFERENCES

(1) Halcrow, M. A. *Spin-Crossover Materials: Properties and Applications*; Wiley, 2013.

(2) Long, J.; Ivanov, M. S.; Khomchenko, V. A.; Mamontova, E.; Thibaud, J.-M.; Rouquette, J.; Beaudhuin, M.; Granier, D.; Ferreira, R. A. S.; Carlos, L. D.; Donnadieu, B.; Henriques, M. S. C.; Paixão, J. A.; Guari, Y.; Larionova, J. Room temperature magnetoelectric coupling in a molecular ferroelectric ytterbium(III) complex. *Science* **2020**, *367*, 671−676.

(3) Ueda, A.; Yamada, S.; Isono, T.; Kamo, H.; Nakao, A.; Kumai, R.; Nakao, H.; Murakami, Y.; Yamamoto, K.; Nishio, Y.; Mori, H. Hydrogen-Bond-Dynamics-Based Switching of Conductivity and Magnetism: A Phase Transition Caused by Deuterium and Electron Transfer in a Hydrogen-Bonded Purely Organic Conductor Crystal. *J. Am. Chem. Soc.* **2014**, *136*, 12184−12192.

(4) Sauvage, J.-P. Transition Metal-Containing Rotaxanes and Catenanes in Motion: Toward Molecular Machines and Motors. *Acc. Chem. Res.* **1998**, *31*, 611−619.

(5) Fittipaldi, M.; Cini, A.; Annino, G.; Vindigni, A.; Caneschi, A.; Sessoli, R. Electric field modulation of magnetic exchange in molecular helices. *Nat. Mater.* **2019**, *18*, 329−334.

(6) Huang, W.; Ma, X.; Sato, O.; Wu, D. Controlling Dynamic Magnetic Properties of Coordination Clusters via Switchable Electronic Configuration. *Chem. Soc. Rev.* **2021**, *50*, 6832−6870.

(7) Miyawaki, A.; Eda, K.; Mochida, T.; Sakurai, T.; Ohta, H.; Nakajima, T.; Takahashi, K. Spin-Crossover-Triggered Linkage Isomerization by the Pedal-like Motion of the Azobenzene Ligand in a Neutral Heteroleptic Iron(III) Complex. *Inorg. Chem.* **2021**, *60*, 12735−12739.

(8) Sato, O. Dynamic molecular crystals with switchable physical properties. *Nat. Chem.* **2016**, *8*, 644−656.

(9) Nakaya, M.; Ohtani, R.; Lindoy, L. F.; Hayami, S. Light-Induced Excited Spin State Trapping in Iron(III) Complexes. *Inorg. Chem. Front.* **2021**, *8*, 484−498.

(10) Zhang, J. L.; Zhong, J. Q.; Lin, J. D.; Hu, W. P.; Wu, K.; Xu, G. Q.; Wee, A. T. S.; Chen, W. Towards single molecule switches. *Chem. Soc. Rev.* **2015**, *44*, 2998−3022.

(11) Tissot, A.; Kesse, X.; Giannopoulou, S.; Stenger, I.; Binet, L.; Riviére, E.; Serre, C. A Spin Crossover Porous Hybrid Architecture for Potential Sensing Applications. *Chem. Commun.* **2019**, *55*, 194−197.

(12) Irie, M.; Fukaminato, T.; Matsuda, K.; Kobatake, S. Photochromism of Diarylethene Molecules and Crystals: Memories, Switches, and Actuators. *Chem. Rev.* **2014**, *114*, 12174−12277.

(13) Bogani, L.; Wernsdorfer, W. Molecular spintronics using single-molecule magnets. *Nat. Mater.* **2008**, *7*, 179−186.

(14) Lefter, C.; Rat, S.; Costa, J. S.; Manrique-Juárez, M. D.; Quintero, C. M.; Salmon, L.; Séguy, I.; Leichle, T.; Nicu, L.; Demont, P.; Rotaru, A.; Molnár, G.; Bousseksou, A. Current Switching Coupled to Molecular Spin-States in Large-Area Junctions. *Adv. Mater.* **2016**, *28*, 7508−7514.

(15) Karuppannan, S. K.; Martín-Rodríguez, A.; Harding, P.; Harding, D. J.; Yu, X.; Tadich, A.; Cowie, B.; Nijhuis, C. A.; Ruiz, E.; Qi, D. Room Temperature Conductance Switching in a Molecular Iron(III) Spin Crossover Junction. *Chem. Sci.* **2021**, *12*, 2381−2388.

(16) Habarakada, U.; Boonprab, T.; Harding, P.; Murray, K. S.; Phonsri, W.; Neville, S. M.; Ahmed, M.; Harding, D. J. Solvent Effects on the Structural and Magnetic Properties of Fe^{III} Spin-Crossover Complexes. *Cryst. Growth Des.* **2022**, *22*, 4895−4905.

(17) Phonsri, W.; Harding, P.; Liu, L.; Telfer, S. G.; Murray, K. S.; Moubaraki, B.; Ross, T. M.; Jameson, G. N. L.; Harding, D. J. Solvent modified spin crossover in an iron(iii) complex: phase changes and an exceptionally wide hysteresis. *Chem. Sci.* **2017**, *8*, 3949−3959.

(18) Martinho, P. N.; Gildea, B.; Harris, M. M.; Lemma, T.; Naik, A. D.; Müller-Bunz, H.; Keyes, T. E.; Garcia, Y.; Morgan, G. G. Cooperative spin transition in a mononuclear manganese(III) complex. *Angew. Chem., Int. Ed.* **2012**, *51*, 12597−12601.

(19) Xue, S.; Guo, Y.; Rotaru, A.; Müller-Bunz, H.; Trzop, E.; Collet, E.; Olah, J.; Garcia, Y.; Morgan, G. G. Spin Crossover Behavior in a Homologous Series of Iron(II) Complexes Based on Functionalized Bipyridyl Ligands. *Inorg. Chem.* **2018**, *57*, 9880−9891.

(20) Hayami, S.; Komatsu, Y.; Shimizu, T.; Kamihata, H.; Lee, Y. H. Spin-crossover in cobalt(II) compounds containing terpyridine and its derivatives. *Coord. Chem. Rev.* **2011**, *255*, 1981−1990.

(21) Muñoz, M. C.; Real, J. A. Thermo-, piezo-, photo- and chemoswitchable spin crossover iron(II)-metallocyanate based coordination polymers. *Coord. Chem. Rev.* **2011**, *255*, 2068−2093.

(22) Neville, S. M.; Halder, G. J.; Chapman, K. W.; Duriska, M. B.; Moubaraki, B.; Murray, K. S.; Kepert, C. J. Guest tunable structure and spin crossover properties in a nanoporous coordination framework material. *J. Am. Chem. Soc.* **2009**, *131*, 12106−12108.

(23) Prins, F.; Monrabal-Capilla, M.; Osorio, E. A.; Coronado, E.; van der Zant, H. S. J. Room-Temperature Electrical Addressing of a Bistable Spin-Crossover Molecular System. *Adv. Mater.* **2011**, *23*, 1545−1549.

(24) Reczynski, M.; Pinkowicz, D.; Nakabayashi, K.; Nather, C.; Stanek, J.; Koziel, M.; Kalinowska-Tluscik, J.; Sieklucka, B.; Ohkoshi, S. I.; Nowicka, B. Room-temperature bistability in a Ni-Fe chain: electron transfer controlled by temperature, pressure, light, and humidity. *Angew. Chem., Int. Ed.* **2021**, *60*, 2330−2338.

(25) Zheng, H.; Meng, Y.-S.; Zhou, G.-L.; Duan, C.-Y.; Sato, O.; Hayami, S.; Luo, Y.; Liu, T. Simultaneous modulation of magnetic and dielectric transition via spin-crossover-tuned spin arrangement and charge distribution. *Angew. Chem., Int. Ed.* **2018**, *57*, 8468−8472.

(26) Estrader, M.; Salinas Uber, J.; Barrios, L. A.; Garcia, J.; Lloyd-Williams, L.; Roubeau, O.; Teat, S. J.; Aromi, G. A Magneto-optical Molecular Device: Interplay of Spin Crossover, Luminescence, Photomagnetism, and Photochromism. *Angew. Chem., Int. Ed.* **2017**, *56*, 15622−15627.

(27) Torres-Cavanillas, R.; Morant-Giner, M.; Escorcia-Ariza, G.; Dugay, J.; Canet-Ferrer, J.; Tatay, S.; Cardona-Serra, S.; Giménez-Marqués, M.; Galbiati, M.; Forment-Aliaga, A.; Coronado, E. Spincrossover nanoparticles anchored on MoS2 layers for hetero-

structures with tunable strain driven by thermal or light-induced spin switching. *Nat. Chem.* **2021**, *13*, 1101−1109.
(28) Shiga, T.; Saiki, R.; Akiyama, L.; Kumai, R.; Natke, D.; Renz, F.; Cameron, J. M.; Newton, G. N.; Oshio, H. A Brønsted-Ligand-Based Iron Complex as a Molecular Switch with Five Accessible States. *Angew. Chem. Int. Ed.* **2019**, *58*, 5658−5662.
(29) Niel, V.; Martinez-Agudo, J. M.; Muñoz, M. C.; Gaspar, A. B.; Real, J. A. Cooperative Spin Crossover Behavior in Cyanide-Bridged Fe(II)-M(II) Bimetallic 3D Hofmann-like Networks (M = Ni, Pd, and Pt). *Inorg. Chem.* **2001**, *40*, 3838−3839.
(30) Cobo, S.; Molnár, G.; Real, J. A.; Bousseksou, A. Multilayer Sequential Assembly of Thin Films That Display Room-Temperature Spin Crossover with Hysteresis. *Angew. Chem., Int. Ed.* **2006**, *45*, 5786−5789.
(31) Gütlich, P.; Gaspar, A. B.; Garcia, Y. Spin state switching in iron coordination compounds. *Beilstein J. Org. Chem.* **2013**, *9*, 342−391.
(32) Brooker, S. Spin crossover with thermal hysteresis: practicalities and lessons learnt. *Chem. Soc. Rev.* **2015**, *44*, 2880−2892.
(33) Lochenie, C.; Schötz, K.; Panzer, F.; Kurz, H.; Maier, B.; Puchtler, F.; Agarwal, S.; Köhler, A.; Weber, B. Spin-Crossover Iron(II) Coordination Polymer with Fluorescent Properties: Correlation between Emission Properties and Spin State. *J. Am. Chem. Soc.* **2018**, *140*, 700−709.
(34) Kawabata, S.; Chorazy, S.; Zakrzewski, J. J.; Imoto, K.; Fujimoto, T.; Nakabayashi, K.; Stanek, J.; Sieklucka, B.; Ohkoshi, S. In Situ Ligand Transformation for Two-Step Spin Crossover in $Fe^{II}[M^{IV}(CN)_8]^{4+}$ (M = Mo, Nb) Cyanido-Bridged Frameworks. *Inorg. Chem.* **2019**, *58*, 6052−6063.
(35) Cruddas, J.; Powell, B. J. Structure-property relationships and the mechanisms of multistep transitions in spin crossover materials and frameworks. *Inorg. Chem. Front.* **2020**, *7*, 4424−4437.
(36) Paez-Espejo, M.; Sy, M.; Boukheddaden, K. Elastic Frustration Causing Two-Step and Multistep Transitions in Spin-Crossover Solids: Emergence of Complex Antiferroelastic Structures. *J. Am. Chem. Soc.* **2016**, *138*, 3202−3210.
(37) Sciortino, N. F.; Zenere, K. A.; Corrigan, M. E.; Halder, G. J.; Chastanet, G.; Létard, J. F.; Kepert, C. J.; Neville, S. M. Four-step iron (II) spin state cascade driven by antagonistic solid-state interactions. *Chem. Sci.* **2017**, *8*, 701−707.
(38) Trzop, E.; Zhang, D.; Piñeiro-Lopez, L.; Valverde-Muñoz, F. J.; Carmen Muñoz, M.; Palatinus, L.; Guerin, L.; Cailleau, H.; Real, J. A.; Collet, E. First Step Towards a Devil's Staircase in Spin-Crossover Materials. *Angew. Chem., Int. Ed.* **2016**, *55*, 8675−8679.
(39) Kucheriv, O. I.; Fritsky, I. O.; Gural'skiy, I. A. Spin crossover in Fe^{II} cyanometallic frameworks. *Inorg. Chim. Acta* **2021**, *521*, 120303.
(40) Delgado, T.; Meneses-Sánchez, M.; Piñeiro-López, L.; Bartual-Murgui, C.; Muñoz, M. C.; Real, J. A. Thermo- and photo-modulation of exciplex fluorescence in a 3D spin crossover Hofmann-type coordination polymer. *Chem. Sci.* **2018**, *9*, 8446−8452.
(41) Munoz, M. C.; Real, J. A. Thermo-, piezo-, photo- and chemo-switchable spin crossover iron(II)-metallocyanate based coordination polymers. *Coord. Chem. Rev.* **2011**, *255*, 2068−2093.
(42) Ahmed, M.; Arachchige, K. S. A.; Xie, Z.; Price, J. R.; Cruddas, J.; Clegg, J. K.; Powell, B. J.; Kepert, C. J.; Neville, S. M. Guest-Induced Multistep to Single-Step Spin-Crossover Switching in a 2-D Hofmann-Like Framework with an Amide-Appended Ligand. *Inorg. Chem.* **2022**, *61*, 11667−11674.
(43) Turo-Cortes, R.; Meneses-Sanchez, M.; Delgado, T.; Bartual-Murgui, C.; Munoz, M. C.; Real, J. A. Coexistence of luminescence and spin-crossover in 2D iron(II) Hofmann clathrates modulated through guest encapsulation. *J. Mater. Chem. C* **2022**, *10*, 10686−10698.
(44) Southon, P. D.; Liu, L.; Fellows, E. A.; Price, D. J.; Halder, G. J.; Chapman, K. W.; Moubaraki, B.; Murray, K. S.; Létard, J.-F.; Kepert, C. J. Dynamic Interplay between Spin-Crossover and Host-Guest Function in a Nanoporous Metal-Organic Framework Material. *J. Am. Chem. Soc.* **2009**, *131*, 10998−11009.
(45) Ni, Z.-P.; Liu, J.-L.; Hoque, N.; Liu, W.; Li, J.-Y.; Chen, Y.-C.; Tong, M.-L. Recent advances in guest effects on spin crossover behavior in Hofmann-type metal-organic frameworks. *Coord. Chem. Rev.* **2017**, *335*, 28−43.
(46) Chorazy, S.; Zakrzewski, J. J.; Magott, M.; Korzeniak, T.; Nowicka, B.; Pinkowicz, D.; Podgajny, R.; Sieklucka, B. Octacyanidometallates for multifunctional molecule-based materials. *Chem. Soc. Rev.* **2020**, *49*, 5945−6001.
(47) Kobylarczyk, J.; Liberka, M.; Stanek, J. J.; Sieklucka, B.; Podgajny, R. Tuning of the phase transition between site selective SCO and intermetallic ET in trimetallic magnetic cyanido-bridged clusters. *Dalton Trans.* **2020**, *49*, 17321−17330.
(48) Wei, R.-M.; Kong, M.; Cao, F.; Li, J.; Pu, T.-C.; Yang, L.; Song, Y.; Zhang, X.-L. Water induced spin-crossover behaviour and magneto-structural correlation in octacyanotungstate(IV)-based iron-(II) complexes. *Dalton Trans.* **2016**, *45*, 18643−18652.
(49) Chorazy, S.; Charytanowicz, T.; Pinkowicz, D.; Wang, J.; Nakabayashi, K.; Klimke, S.; Renz, F.; Ohkoshi, S.; Sieklucka, B. Octacyanidorhenate(V) Ion as an Efficient Linker for Hysteretic Two-Step Iron(II) Spin Crossover Switchable by Temperature, Light, and Pressure. *Angew. Chem., Int. Ed.* **2020**, *59*, 15741−15749.
(50) Magott, M.; Ceglarska, M.; Rams, M.; Sieklucka, B.; Pinkowicz, D. Magnetic interactions controlled by light in the family of Fe(II)-M(IV) (M = Mo, W, Nb) hybrid organic-inorganic frameworks. *Dalton Trans.* **2022**, *51*, 8885−8892.
(51) Arai, M.; Kosaka, W.; Matsuda, T.; Ohkoshi, S. Observation of an Fe(II) spin-crossover in an iron octacyanoniobate-based magnet. *Angew. Chem., Int. Ed.* **2008**, *47*, 6885−6887.
(52) Ohkoshi, S.; Takano, S.; Imoto, K.; Yoshikiyo, M.; Namai, A.; Tokoro, H. 90-degree optical switching of output second-harmonic light in chiral photomagnet. *Nat. Photonics* **2014**, *8*, 65−71.
(53) Ohkoshi, S.; Imoto, K.; Tsunobuchi, Y.; Takano, S.; Tokoro, H. Light-induced spin-crossover magnet. *Nat. Chem.* **2011**, *3*, 564−569.
(54) Pinkowicz, D.; Rams, M.; Mišek, M.; Kamenev, K. V.; Tomkowiak, H.; Katrusiak, A.; Sieklucka, B. Enforcing Multifunctionality: A Pressure-Induced Spin-Crossover Photomagnet. *J. Am. Chem. Soc.* **2015**, *137*, 8795−8802.
(55) Charytanowicz, T.; Zakrzewski, J. J.; Dziedzic-Kocurek, K.; Chorazy, S.; Sieklucka, B. The ON-OFF switching of thermal spin crossover by interstitial solvent exchange in a layered Re^{V}-CN-Fe^{II} coordination framework. *J. Appl. Phys.* **2021**, *129*, 143902.
(56) Arczyński, M.; Stanek, J.; Sieklucka, B.; Dunbar, K. R.; Pinkowicz, D. Site-Selective Photoswitching of Two Distinct Magnetic Chromophores in a Propeller-Like Molecule To Achieve Four Different Magnetic States. *J. Am. Chem. Soc.* **2019**, *141*, 19067−19077.
(57) Chorazy, S.; Podgajny, R.; Nakabayashi, K.; Stanek, J.; Rams, M.; Sieklucka, B.; Ohkoshi, S. Fe^{II} Spin-Crossover Phenomenon in the Pentadecanuclear $\{Fe_9[Re(CN)_8]_6\}$ Spherical Cluster. *Angew. Chem., Int. Ed.* **2015**, *54*, 5093−5097.
(58) Chorazy, S.; Stanek, J. J.; Kobylarczyk, J.; Ohkoshi, S.; Sieklucka, B.; Podgajny, R. Modulation of the Fe^{II} spin crossover effect in the pentadecanuclear $\{Fe_9[M(CN)_8]_6\}$ (M = Re, W) clusters by facial coordination of tridentate polyamine ligands. *Dalton Trans.* **2017**, *46*, 8027−8036.
(59) Sheldrick, G. M. *SHELXT* - Integrated space-group and crystal-structure determination. *Acta Crystallogr.* **2015**, *A71*, 3−8.
(60) Llunell, M.; Casanova, D.; Cirera, J.; Bofill, J.; Alemany, P.; Alvarez, S.; Pinsky, M.; Avnir, D. Program for the calculation of continuous shape measures of polygonal and polyhedral molecular fragments. *SHAPE v. 2.1*; University of Barcelona: Barcelona, 2013.
(61) Casanova, D.; Cirera, J.; Llunell, M.; Alemany, P.; Avnir, D.; Alvarez, S. Minimal Distortion Pathways in Polyhedral Rearrangements. *J. Am. Chem. Soc.* **2004**, *126*, 1755−1763.
(62) Galland, A.; Dupray, V.; Berton, B.; Morin-Grognet, S.; Sanselme, M.; Atmani, H.; Coquerel, G. Spotting Conglomerates by Second Harmonic Generation. *Cryst. Growth Des.* **2009**, *9*, 2713−2718.
(63) Mercier, N.; Barres, A.-L.; Giffard, M.; Rau, I.; Kajzar, F.; Sahraoui, B. Conglomerate-to-True-Racemate Reversible Solid-State

https://doi.org/10.1021/acs.cgd.2c01462
Cryst. Growth Des. 2023, 23, 4052−4064

Transition in Crystals of an Organic Disulfide-Based Iodoplumbate. *Angew. Chem., Int. Ed.* **2006**, *45*, 2100−2103.
(64) Nalla, V.; Medishetty, R.; Wang, Y.; Bai, Z.; Sun, H.; Wei, J.; Vittal, J. J. Second harmonic generation from the 'centrosymmetric' crystals. *IUCrJ.* **2015**, *2*, 317−321.
(65) Rajesh Goud, N.; Zhang, X.; Bredas, J.-L.; Coropceanu, V.; Matzger, A. J. Discovery of Non-linear Optical Materials by Function-Based Screening of Multi-component Solids. *Chem.* **2018**, *4*, 150−161.
(66) Shi, R.; Han, X.; Xu, J.; Bu, X.-H. Crystalline Porous Materials for Nonlinear Optics. *Small* **2021**, *17*, 2006416.
(67) Huang, Y.; Meng, X.; Gong, P.; Lin, Z.; Chen, Z.; Qin, J. A study on $K_2SbF_2Cl_3$ as a new mid-IR nonlinear optical material: new synthesis and excellent properties. *J. Mater. Chem. C* **2015**, *3*, 9588−9593.
(68) Moskwa, M.; Bator, G.; Rok, M.; Medycki, W.; Miniewicz, A.; Jakubas, R. Investigations of organic-inorganic hybrids based on homopiperidinium cation with haloantimonates(III) and halobismuthates(III). Crystal structures, reversible phase transitions, semiconducting and molecular dynamic properties. *Dalton Trans.* **2018**, *47*, 13507−13522.
(69) Peksa, P.; Zaręba, J. K.; Ptak, M.; Mączka, M.; Gągor, A.; Pawlus, S.; Sieradzki, A. Revisiting a Perovskite-like Copper-Formate Framework NH4[Cu(HCOO)3]: Order-Disorder Transition Influenced by Jahn-Teller Distortion and above Room-Temperature Switching of the Nonlinear Optical Response between Two SHG-Active States. *J. Phys. Chem. C* **2020**, *124*, 18714−18723.
(70) Train, C.; Nuida, T.; Gheorghe, R.; Gruselle, M.; Ohkoshi, S. Large Magnetization-Induced Second Harmonic Generation in an Enantiopure Chiral Magnet. *J. Am. Chem. Soc.* **2009**, *131*, 16838−16843.
(71) Jankowski, R.; Zakrzewski, J. J.; Zychowicz, M.; Wang, J.; Oki, Y.; Ohkoshi, S.; Chorazy, S.; Sieklucka, B. SHG-active NIR-emissive molecular nanomagnets generated in layered neodymium(III)-octacyanidometallate(IV) frameworks. *J. Mater. Chem. C* **2021**, *9*, 10705−10717.
(72) Kosaka, W.; Nuida, T.; Hashimoto, K.; Ohkoshi, S. Crystal structure, magnetic properties, and second harmonic generation of a three-dimensional pyroelectric cyano-bridged Mn-Mo complex. *Bull. Chem. Soc. Jpn.* **2007**, *80*, 960−962.
(73) Yu, J.; Cui, Y.; Wu, C.; Yang, Y.; Wang, Z.; O'Keefe, M.; Chen, B.; Qian, G. Second-Order Nonlinear Optical Activity Induced by Ordered Dipolar Chromophores Confined in the Pores of an Anionic Metal-Organic Framework. *Angew. Chem., Int. Ed.* **2012**, *51*, 10542−10545.
(74) Komine, M.; Chorazy, S.; Imoto, K.; Nakabayashi, K.; Ohkoshi, S. SHG-active Ln^{III}-$[Mo^{I}(CN)_5(NO)]^{3-}$ (Ln = Gd, Eu) magnetic coordination chains: a new route towards non-centrosymmetric molecule-based magnets. *CrystEngComm* **2017**, *19*, 18−22.
(75) Kumar, K.; Stefanczyk, O.; Nakabayashi, K.; Imoto, K.; Ohkoshi, S. Studies of Er(III)-W(V) compounds showing nonlinear optical activity and single-molecule magnetic properties. *CrystEngComm* **2019**, *21*, 5882−5889.
(76) Hu, T.; Hu, C.; Li, Y.; Meng, L.; Xie, Y.; Liao, M.; Zhong, G.; Lu, C.-Z. Synthesis and characterization of a nanocluster-based silver(I) tert-butylethynide compound with a large second-harmonic generation response. *Nanoscale* **2020**, *12*, 11847−11857.
(77) Wan, Y.; Wang, J.; Shu, H.; Cheng, B.; He, Z.; Wang, P.; Xia, T. Series of Luminescent Lanthanide MOFs with Regular SHG Performance. *Inorg. Chem.* **2021**, *60*, 7345−7350.

https://doi.org/10.1021/acs.cgd.2c01462
Cryst. Growth Des. 2023, 23, 4052−4064